



Ultra-efficient generation of time-energy entangled photon pairs in an InGaP photonic crystal cavity

Alexandre Chopin ^{1,2,6}✉, Andrea Barone ^{3,6}, Inès Ghorbel¹, Sylvain Combrié¹, Daniele Bajoni⁴, Fabrice Raineri^{2,5}, Matteo Galli³ & Alfredo De Rossi¹

The typical approaches to generate heralded single photons rely on parametric processes, with the advantage of generating highly entangled states at the price of a random pair emission. To overcome this limit, degenerate spontaneous Four-Wave-Mixing is a reliable technique which combines two pump photons into a pair of signal and idler photons via Kerr nonlinear optical effect. By exploiting the intrinsic small confinement volume and thermally tuning the resonances of a 20 μm -long Photonic Crystal cavity, we efficiently generate time-energy entangled photon pairs and heralded single photons at a large maximum on-chip rate of 22 MHz, using 36 μW of pump power. We measure time-energy entanglement with net visibility up to 96.6 % using 1 second integration time constant. Our measurements demonstrate the viability of Photonic Crystal cavities to act as an alternative and efficient photon pair source for quantum photonics.

¹Thales Research and Technology, Campus Polytechnique, 1 avenue Augustin Fresnel, 91767 Palaiseau, France. ²Centre de Nanosciences et de Nanotechnologies, CNRS, Université Paris Saclay, Palaiseau, France. ³Dipartimento di Fisica, Università di Pavia, Via Bassi 6, 27100 Pavia, Italy. ⁴Dipartimento di Ingegneria Industriale e dell'Informazione, Università di Pavia, Via Adolfo Ferrata 5, 27100 Pavia, Italy. ⁵Université Côte d'Azur, Institut de Physique de Nice, CNRS-UMR 7010, Sophia Antipolis, France. ⁶These authors contributed equally: Alexandre Chopin, Andrea Barone. ✉email: alexandre.chopin@universite-paris-saclay.fr

The development of quantum technologies promises a paradigm change in the way we process and encode information, leading to a great leap towards encryption safety^{1,2} and exponential computational advantage^{3–5}. Integrated photonics can provide solutions to address the generation and manipulation of entangled states of light on-chip and at room temperature^{6,7}. Single photons can serve as the fundamental photonic qubit, or can be manipulated to construct more general entangled states; therefore, efficient single photon sources (SPSs) are required. Different routes have been explored in this regard, for example, the emission of defects in diamonds or semiconductors^{8–10}, artificial solid-state quantum emitters such as quantum dots^{11–13}, and parametric processes exploiting intrinsic material nonlinearity. Correlated photon pairs spontaneously generated via parametric processes can be used to build heralded SPSs^{14–18}, in which the detection of one photon in one input channel heralds the presence of its twin photon in the other. Such processes can provide highly coherent entangled states but, relying on spontaneous processes, the pair emission is random and the source is probabilistic, making it crucial to achieve the highest generation efficiency. Our system exploits degenerate spontaneous four-wave-mixing (FWM) that is an ultrafast Kerr optical nonlinear effect where two pump photons (at frequency ν_p) are converted into a pair of signal (ν_s) and idler (ν_i) photons. Because of energy conservation (Fig. 1a), $2h\nu_p = h\nu_s + h\nu_i$, signal and idler photons are emitted symmetrically relative to the pump, as in Fig. 1b. As a consequence, resonant enhancement can only be achieved if at least three resonances of the cavity (at frequencies ν_- , ν_0 and ν_+) are strictly equispaced. This is called the triply resonant configuration and under this condition, the internal pair generation rate (number of pairs generated per second) scales as^{19,20} $R \propto (n_2^2 Q^3 / V^2) P^2$; with n_2 the Kerr nonlinear index, Q the average quality factor of the three modes defined as $Q^3 = Q_0^2 \sqrt{Q_- Q_+}$, V the volume of the resonator, and

P the pump power delivered to the cavity. Ring resonators have gained huge interest for quantum optics as they own the adequate properties (high Q-factor, equispaced modes, ...) for triply resonant FWM and are now easily integrated on-chip. Time-energy entangled photon pairs have already been demonstrated in silicon photonics²¹ and III–V semiconductors as InP²² and recently AlGaAs²³. This last material has shown efficiency R/P^2 as large as 20 GHz/mW² mainly due to a very large Q-factor up to 1.24×10^6 , making it the current state-of-the-art integrated photon pair source based on semiconductors via FWM. Larger efficiency is reachable by increasing the Q-factor or further decreasing the volume of the cavity, but bending losses set a lower bound to the size of the ring.

Yet, whether entangled photons can be generated using a radically different kind of resonator where the field is strongly localized within the scale of the wavelength, has not been investigated at all to the best of our knowledge. We consider a photonic crystal (PhC) cavity where the very large index contrast leads to a very strong confinement of light²⁴. Moreover, the generation of time-correlated photons has just been reported²⁵. PhC are dielectric sub-wavelength structures where Bragg scattering inhibits the propagation of light within a large angular and spectral range. This enables the strong localization of the field²⁶ to the scale of the wavelength. This is a fundamental difference with respect to other dielectric structures, which is appreciated when considering the possibility of manipulating each single mode. This gives superior control on the parametric processes, either desired or undesired, and represents a considerable advantage when each emitted photon counts. Practical PhC are one or two-dimensional periodic structures with imperfect bandgap, yet they are still able to confine a small number of non-degenerate modes within a volume $\approx (\lambda/2n)^3$ (λ being the wavelength and n the index of the medium) while ensuring a large Q-factor²⁷, up to 10 million on silicon²⁸ and one million in III–V

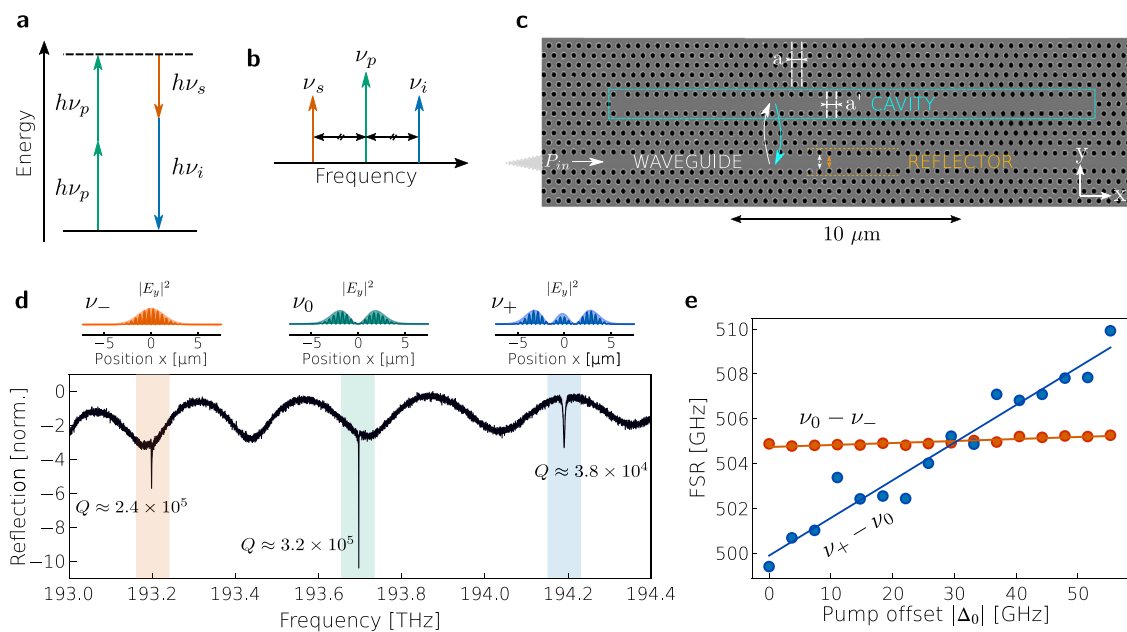


Fig. 1 Bichromatic photonic crystal cavity. **a** Schematic of the energy diagram for degenerate FWM, where two pump photons are converted into a signal and an idler photon. Frequencies (ν_p, ν_s , and ν_i) are dictated by energy conservation $2\nu_p = \nu_s + \nu_i$ and h is Planck constant. **b** Corresponding schematic of the emission spectra, showing emission at ν_s and ν_i symmetrically to ν_p . **c** SEM image of the cavity describing the different elements of the design. a and a' are the periods of the holes. P_{in} is for the input power in the waveguide. White and orange arrows guide the eyes to see the shift of the lines of holes forming the reflector. **d** Reflection spectrum (measured with OCT) of the cavity limited to the first three modes of frequencies ν_-, ν_0 , and ν_+ used here for photon pair generation. The corresponding spatial profile of the modes $|E_y|^2$ are given above. Q is the Q-factor. **e** Thermal tuning, the evolution of the Free Spectral Range $\nu_0 - \nu_-$ (red points) and $\nu_+ - \nu_0$ (blue points) as a function of the pump offset $\Delta_0 = \nu_p - \bar{\nu}_0$. Colored circles are measured with pump-probe OCT and continuous lines are linear fit of the data. Equispaced configuration is reached at $\Delta_0 = 31$ GHz.

semiconductors²⁹. Considering the strong dependence of the photon pair generation efficiency on these parameters, PhC cavities are very attractive for quantum light generation via FWM²⁵, provided that the free spectral range is controlled with very high accuracy. The first demonstration of spontaneous emission via FWM was reported by Azzini et al.³⁰ by coupling three identical nanobeam cavities with Q-factor $\approx 5 \times 10^3$, which in the tight-binding approximation, would lead to three symmetrically spaced resonances. Unfortunately, the dispersive nature of the coupling in PhC³¹ and ring resonators³² fundamentally leaves a non-zero dispersion $\Delta_2 = (\nu_+ - \nu_0) - (\nu_0 - \nu_-)$. This effect is not severe if the Q-factor is moderate (e.g. $\approx 5 \times 10^3$) but absolutely needs to be controlled if a much larger Q is to be harnessed. We consider another approach that consists in designing a cavity which, by construction, results in evenly spaced modes²⁹. However, fabrication tolerances contribute with additional random frequency shift, affecting inhomogeneously the different resonances due to their non-degenerate nature. It can be corrected with post-fabrication trimming, like in Silicon³³. Owing to a self-tuning technique, we demonstrated time-correlated photon pairs²⁵ and optical parametric oscillations³⁴ with pump power in the tens of microWatt level. Here, we will show that our triply resonant PhC cavity generates correlated photon pairs with very large efficiency, that are time-energy entangled and allow heralded single-photon emission.

Results

Bichromatic photonic crystal resonator. The resonator design is based on the so-called bichromatic lattice³⁵ and is shown in Fig. 1c. Details on the cavity are given in Methods: Sample design, fabrication, and characterization. The purpose of this design is to create an effective parabolic potential for the optical field. Analogously to the quantum harmonic oscillator, modes are equispaced in frequencies as desired for triply resonant FWM; and their spatial profiles are described in good approximation by Hermite–Gauss functions.

The field distributions for the first three modes of the resonator, that will be used in the following are shown in Fig. 1d, along with the reflection spectrum of the resonator. This is measured using optical coherent tomography (OCT), a coherent spectral technique providing the phase and the amplitude of the spectrum. The parameters of the triplet of resonances are extracted following the procedure in ref. ²⁹. In the specific case of the resonator considered here, the Q-factors of the signal and idler modes are different: $Q_- = 3.8 \times 10^4$ and $Q_+ = 2.4 \times 10^5$, giving an average (defined above) of 2.09×10^5 . The free spectral range is not constant, leading to a deviation from the required frequency matching condition defined as $\Delta_2 = (\nu_+ - \nu_0) - (\nu_0 - \nu_-) = -5$ GHz. This mismatch is comparable with the largest linewidth of the triplet (≈ 5 GHz); therefore, either post-fabrication tuning³³ or dynamic tuning are necessary to bring the cavity to the triply resonant configuration.

In the present work, we resort to the latter option, more precisely, self-thermal tuning. This technique has already been discussed and detailed in refs. ^{25,34,36}. It is based on the differential thermo-optic effect that originates from the inhomogeneous spatial distribution of the mode profiles and their consequently different overlaps with a thermal gradient. The aftermath of inhomogeneous temperature in the cavity is a different frequency shift for each mode. Here, the thermal gradient is generated via residual linear absorption through the pump mode. Experimentally, the frequency ν_p of a CW pump laser is gradually shifted to get on resonance with the pump mode at frequency $\bar{\nu}_0$ (“—” indicates the frequency without thermal

tuning). We introduce the pump offset $\Delta_0 = \nu_p - \bar{\nu}_0$ to express the shift of the pump laser. As $\Delta_0 < 0$, the laser starts to be partially resonant with the pump mode allowing energy transfer from the laser to the cavity via the pump mode. The effect of the differential spectral shift of the modes is that as Δ_0 changes, $\nu_0 - \nu_-$ and $\nu_+ - \nu_0$ eventually equalize, which is shown in Fig. 1e using the pump-probe OCT^{25,29} technique. We note that the cavity is kept in the upper (on resonance) branch of the thermal bistable cycle, which closes when $\Delta_0 = \Delta_b$. This condition, not shown in this particular plot, represents a non-equilibrium point where any additional spectral shift is no longer sustained by the thermo-refractive effect. Consequently, aligning the modes requires a minimum pump power (estimated here to be $\approx 20 \mu\text{W}$) that increases with the initial mismatch. It is then possible to operate at low power only when using resonance triplets with a low initial mismatch.

Internal generation rate. First and foremost, the internal pair generation rate R is measured (see Methods: Experimental setups). Indeed, the pump laser used for thermal tuning is also used to generate the photon pairs via spontaneous FWM (SFWM). They are collected by the same lensed fiber and split into two different channels using Dense Wavelength Division Multiplexing, whose frequencies are aligned with the signal and idler ones. For that, the temperature of the sample is set to 32 °C. Each of them is followed by a cascaded bandpass filter with a central frequency matching signal or idler frequency in order to gain additional filtering of the remaining pump photons. Detection is accomplished using superconducting nanowire single-photon detectors, with a quantum efficiency of $\approx 85\%$, connected to a time correlator. Photons’ arrival times are measured and represented in a typical histogram shown in Fig. 2a, after 1 s of integration. It clearly exhibits a main peak corresponding to photon pairs arriving at the detectors over a wideband background, which can be the result of broken signal/idler pairs, the emission of multiple pairs or parasitic processes like Raman scattering in the input waveguide or in the filtering stage²¹. This coincidence peak is not symmetric, that we account for the unbalanced Q-factors. In order to prove that, the coincidence peak is fitted using a model taking into account these unbalanced Q-factors, from which we clearly recover the shape of the peak with the exact Q-factors (see Methods: Coincidence peak fitting). The number of coincidences per second, R_{det} is extracted by integrating over the full-width-half-maximum (FWHM) of the peak. Taking into account the losses between the output of the cavity and detectors (α_s and α_i), estimated to be 12 and 12.84 dB (see Methods: Experimental setups), we infer the internal pair generation rate²⁰ $R = R_{\text{det}} / (\alpha_s \alpha_i)$. This measurement has been performed for different values of the pump offset Δ_0 . As shown in Fig. 2b, the internal pair generation rate increases as the modes are tuned to the triply resonant configuration, up to a maximum of 22 MHz, corresponding to a large measured coincidence rate of 70 kHz. We note that the maximum of generation rate does not exactly correspond to the triply resonant condition (details in ref. ²⁵). We can also infer the amount of effective pump power (Fig. 2c) transferred to the cavity P_0 , with the power in the waveguide P_c and the pump offset at which the bistable jump occurs Δ_b : $P = (\Delta_0 / \Delta_b) P_c$. This effective power can be interpreted as the necessary amount of power required to obtain the corresponding internal generation rate. In order to resolve the entire evolution, $P_c = 56 \mu\text{W}$ have been sent in the waveguide. Finally, we calculate the efficiency. The maximum internal generation rate is obtained for $P = 36 \mu\text{W}$, that gives a maximal efficiency R/P^2 of $16 \pm 1 \text{ GHz/mW}^2$.

Time-energy entanglement. The original idea to exploit energy and time correlation to test non-local quantum correlations was

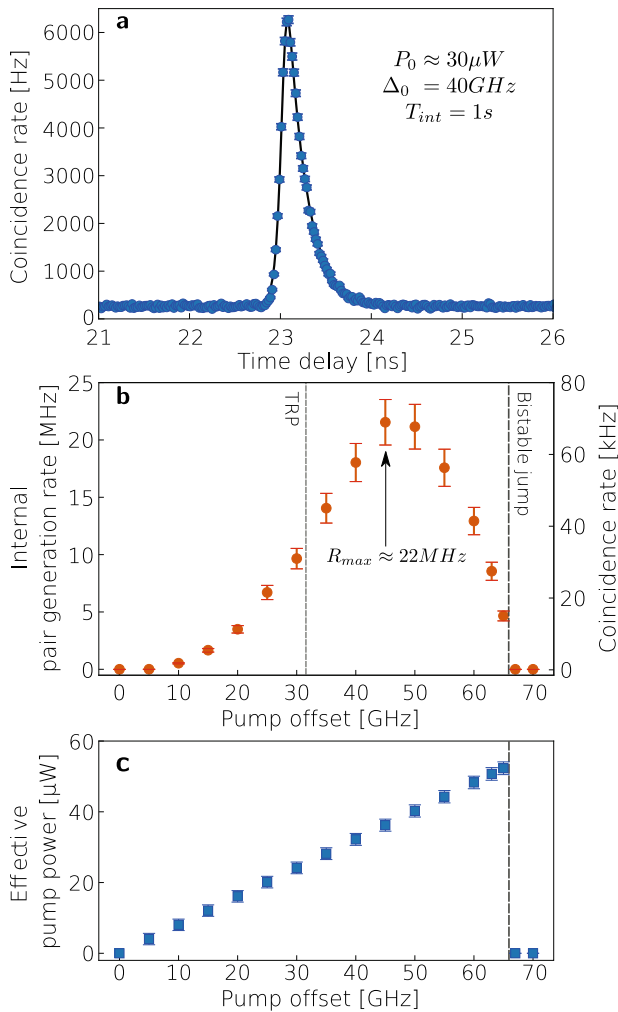


Fig. 2 Time-correlated photon pairs. **a** Coincidence histogram (blue squares) obtained for an effective pump power in the cavity of $P_0 \approx 30 \mu\text{W}$ after $T_{\text{int}} = 1 \text{ s}$ of integration. Δ_0 is the pump offset. The main peak is thus fitted (black line) using the model (detailed in Methods: Coincidence peak fitting) to extract the number of coincidences. **b** On-chip pair generation rate R and the corresponding coincidence rate R_{det} as a function of Δ_0 . Vertical lines denote the point of triply resonant configuration (TRP) and bistable jump. The black arrow indicates the maximal measured internal generation rate R_{max} . Error bars are due to uncertainty on the measured coincidence rate, namely a Poisson distribution. **c** Evolution of the effective pump power P_0 as a function of the pump offset Δ_0 .

suggested in ref. 37. In this seminal paper, two photons emitted in an atomic cascade process are used to test Bell’s inequality. Nowadays, systems based on parametric processes, like the one presented in this work, are most commonly exploited^{20,22,23}. The nonlinear medium in the PhC cavity is pumped with a highly coherent ($\tau_{\text{coh}} \approx 10 \mu\text{s}$) laser at a central frequency ν_p . Photon pairs are simultaneously generated via SFWM, but their emission time is undetermined within the coherence time of the pump, because the coherence time associated with the targeted resonances, 210 and 48 ps for ν_- and ν_+ respectively, is much shorter than the pump one. If the pairs encounter an unbalanced Mach–Zehnder interferometer, the output state of the pair can be written on the path basis, being $|L\rangle$ and $|S\rangle$ the single photon long and short path state, respectively. When the photons of the pair take different paths, $|LS\rangle$ or $|SL\rangle$, they can be distinguished from their time correlations and the states are separable. If, conversely, the two photons take the same path in the interferometer, the state is described by the

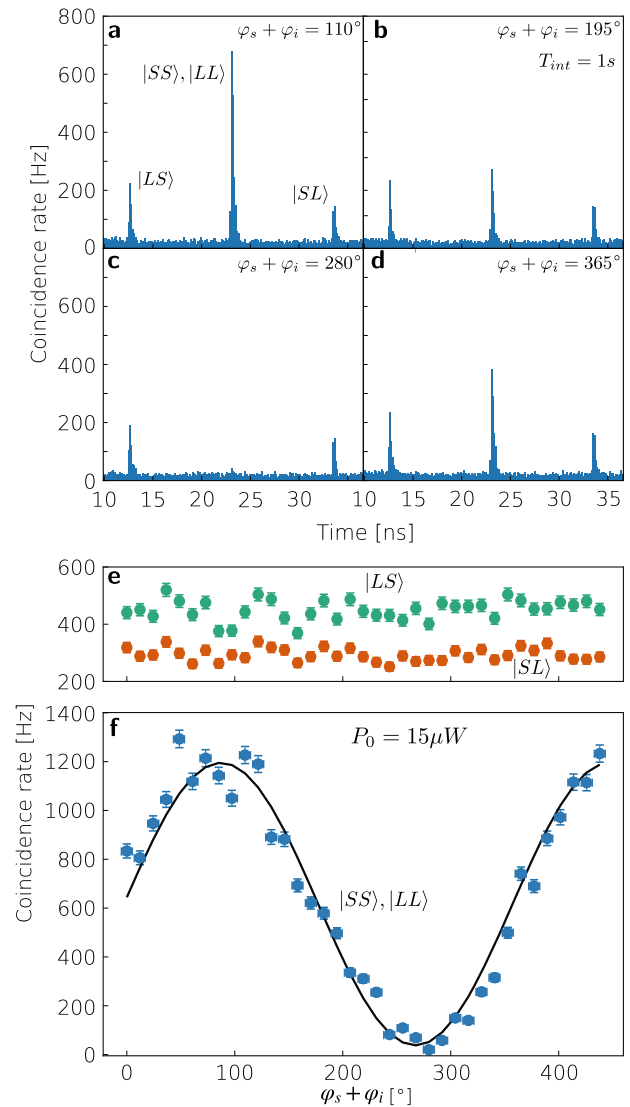


Fig. 3 Time-energy entanglement. **a–d** Coincidence histograms after $T_{\text{int}} = 1 \text{ s}$ integration for different values of the phase acquired by the signal and idler photons in the interferometer $\varphi_s + \varphi_i$. The paths of the photons are shown in the first histogram (S short and L long). **e, f** Coincidence rate for the side peaks (green and red circles) and for the central peak (blue circles), respectively, as a function of $\varphi_s + \varphi_i$. The black curve is fitted with a sinusoidal function to extract the visibility of the fringes caused by two-photon interference. This measurement is obtained for $P_0 = 15 \mu\text{W}$ of pump power. Vertical error bars refer to the standard deviation of a Poisson distribution and horizontal ones to uncertainty on the photon pair phase.

entangled state $|\psi\rangle = (|SS\rangle + \exp[i(\varphi_s + \varphi_i)]|LL\rangle)/\sqrt{2}$, where φ_s and φ_i are the additional phase acquired for each photon of the pair in the long arm of the interferometer, respectively. As the photons result from a parametric conversion, this phase inherits the coherence of the pump. As a result, it will yield an interference in the count rates with a global phase dependence, $\varphi_{s+i} = \varphi_s + \varphi_i$, even though the interferometer unbalance is larger than the coherence time associated with the resonances of the pair.

Time-energy entangled photon pairs have been measured for three different pump powers. Figure 3 shows the results for $P_0 = 15 \mu\text{W}$, corresponding to an internal generation rate $R = 3 \text{ MHz}$. Four coincidence histograms for different values of the relative signal and idler photon phase φ_{s+i} are displayed in Fig. 3a–d obtained after only 1 s of integration. On the one hand,

Table 1 Time-energy entanglement for different effective pump powers.

Type	P_0 [μW]	T_{int} [s]	V_{raw} [%]	V_{net} [%]	$(V_{\text{raw}} - V_{\text{bell}})/\sigma_V$
B	15	1	93.88 \pm 4.07	96.58 \pm 4.19	5.7
B	23	1	89.22 \pm 4.11	91.79 \pm 4.23	4.5
B	36	1	77.13 \pm 1.98	79.35 \pm 2.04	3.2
N	250	30	93.1 \pm 3.4	95.78 \pm 3.49	6.6

T_{int} is the integration time, V_{raw} (V_{net}) is the raw (net) visibility, and σ_V is the uncertainty on the raw visibility. P_0 is the effective pump power. B stands for Bichromatic and N for Nanobeam.

the side peaks that correspond to photons taking $|SL\rangle$ or $|LS\rangle$ path sequence are indeed independent of the phase. On the other hand, the number of coincidences in the central peak, due to photons taking indistinguishable paths ($|SS\rangle$ and $|LL\rangle$), is oscillating with the phase. In Fig. 3e, independent phase evolution of the side peaks is confirmed, while oscillations of the central one are clear over more than 2π in Fig. 3f. The data are fitted using a sinusoidal function (see Methods: Bell curve data extraction), from which the raw visibility V_{raw} is extracted. In Fig. 3f, it is measured to be $V_{\text{raw}} = 93.88 \pm 4.07\%$, violating Bell inequalities by 5.7 standard deviations, proving the entangled nature of the photon pairs. As the pair generation rate R increases, the visibility decreases and drops to $79.81 \pm 1.98\%$ at maximum efficiency due to large increase in the background scaling with P^4 , which is a fundamental limitation due to the statistical properties of the emission process. Finally, the raw visibility is corrected using the one of the interferometer \mathcal{V} . It is directly measured by introducing the pump laser in the Mach–Zehnder and measuring first-order interference visibility. Here, $\mathcal{V} = 0.972 \pm 0.001$ and so the net visibility is $V_{\text{net}} = V_{\text{raw}}/\mathcal{V}$. Results are summarized in Table 1, including also the result obtained with a PhC nanobeam cavity on a different experimental setup (See Supplementary Note 1) and whose photon pair emission properties are detailed in ref. 25. Time-energy entangled photon pairs have thus been demonstrated with net visibility as high as $V_{\text{net}} = 96.6\%$ with $15 \mu\text{W}$ pump power.

Heralded single-photon emission. In order to show that the entangled photons are emitted as single pairs, the heralded second-order correlation function $g_h^{(2)}$ has been measured. The channel with the higher emission rate, v_i , has been chosen as the herald, and on the other channel is performed a conditioned Hanbury Brown–Twiss experiment (see Methods: Experimental setups), feeding light to a 50:50 beam-splitter and sending the output to two distinct Superconducting nanowire single-photon detectors. The $g_h^{(2)}$ can be written in terms of coincidence rate³⁸

$$g_h^{(2)}(\tau) = \frac{R_{i12}(\tau)}{R_{i1}^{(1)}(0)R_{i2}^{(2)}(\tau)} R_i(0), \quad (1)$$

$R_{i12}(\tau)$ being the rate of triple coincidences at delay τ , and R_{i1} , R_{i2} the number of double coincidences between the idler photon and the signal photon in arm 1 or 2 of the Hanbury Brown–Twiss setup, respectively. The expression in eq. (1) can be averaged in time and expressed in terms of measured counts. In this work, a 3-h-long integration leads to the curve depicted in Fig. 4 where the value of the $g_h^{(2)}(0) \simeq 0.17 \pm 0.02$ is a clear sign of the anti-bunched statistic of the emitted state. Yet, the $g_h^{(2)}(0)$ is not as low as achieved in other systems (see Table 2). The reason is that we measured $g_h^{(2)}(0)$ with the pump power level set for maximum pair emission rate, which was dictated by the need to limit the measurement time to a few hours. In this condition, the

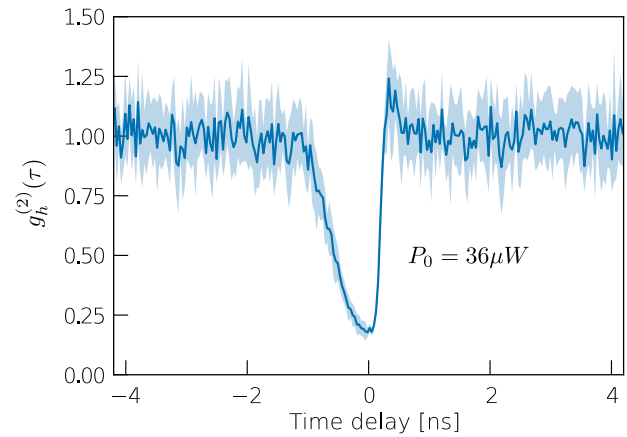


Fig. 4 Heralded single-photon emission. Heralded second-order correlation function showing a $g_h^{(2)}(0) = 0.17 \pm 0.02$; measured at pump power in the cavity $P_0 = 36 \mu\text{W}$. The shaded region corresponds to 1 standard deviation.

probability of multiple pairs emission is high, which also explains the low measured CAR ≈ 10 . To gain more insight, we have measured the second-order self-correlation $g^{(2)}(0)$ of the heralded channel (See Supplementary Note 2), which is directly linked to the purity P and the Schmidt number K :

$$P = \frac{1}{K} = g^{(2)}(0) - 1. \quad (2)$$

As we measure $g^{(2)}(0) = 1.58$, the purity is $58 \pm 1.7\%$, which confirms multiple pairs emission. Hence, lower $g_h^{(2)}(0)$ is expected by repeating the measurement at a lower pair emission rate, as shown in ref. 39.

Discussion

This work shows that PhC cavities are a different and competitive platform for the generation of quantum states of light. First, the performances of our InGaP PhC source are compared to other semiconductor-based microresonators for photon pair generation via SFWM as shown in Fig. 5. The figure compares the performances as a photon pair source of the nanobeam cavity introduced in ref. 25 and the bichromatic cavity discussed here with some landmark results reported in the literature. We consider the generation efficiency R/P^2 , the ratio of the internal pair generation rate over the square of the on-chip pump power as a function of a figure of merit $M \propto (n_2^2 Q^3)/V^2$ which represents the expected scaling with the material nonlinearity, the Q-factor and the nonlinear interaction volume. This figure of merit is normalized to the value corresponding to the performances of the AlGaAs nonlinear ring²³. The Q-factors and other parameters differ considerably, yet the expected scaling with the figure of merit M is followed rather well. A large on-chip generation efficiency, up to 16 GHz/mW^2 , is achieved with the PhC cavity, which is very close to the current state-of-the-art, AlGaAs ring resonator (20 GHz/mW^2) and so, much higher than the other sources. We point out that the smaller Q-factor in the PhC (2.09×10^5 , to be compared with 1.24×10^6 in the AlGaAs ring resonator) and the smaller nonlinearity of our material InGaP are compensated by the much smaller nonlinear volume of the cavity ($5.7 \mu\text{m}^3$, see ref. 34). Thus, the self-tuning technique used here allows to systematically achieve the maximum efficiency, consistently with the scaling. This implies that a further order of magnitude increase in the efficiency is expected, considering Q-factors are twofold larger than in this sample (7×10^5 , as reported in ref. 36). Still, in order to access the ultra-low pump

Table 2 Photon pair sources via resonant parametric processes (SPDC and SFWM) in microresonators.

Material	Geometry	Process	Q	Footprint [μm^2]	R @1mW [GHz]	Visibility	$g_h^{(2)}(0)$ (@R [MHz])	Ref.
LiNbO ₃	Disk	SPDC	2.9×10^5	6800	5.13	$96.5 \pm 1.9\%$	0.0098 ± 0.0021 (70.2)	48
PPLN	Ring	SPDC	1.0×10^5	9500	2.7	x	0.007 ± 0.0016 (5)	39
AlN	Ring	SPDC	1.1×10^5	1960	0.0058	x	0.088 ± 0.004 (5.9)	49
InGaP	Ring	SPDC	1.1×10^5	79	27.5	x	x	40
AlGaAs	Ring	SFWM	1.2×10^6	608	20	$97.1 \pm 0.6\%$	0.004 ± 0.01 (1)	23
Si	Ring	SFWM	9.2×10^4	314	0.15	$98.9 \pm 0.6\%$	0.0053 ± 0.021 (0.02)	41
Si	Ring	SFWM	3×10^4	9000	0.0026	$98.0 \pm 4.1\%$ (raw)	x	42
Si ₃ N ₄	Ring	SFWM	2.0×10^6	42000	0.004	$90 \pm 7\%$	x	50
InP	Ring	SFWM	4.2×10^4	1810	0.145	$78.4 \pm 2.0\%$	x	22
InGaP	Ring	SFWM	4.0×10^4	2830	0.003	x	x	25
InGaP	PhC (N)	SFWM	4.0×10^4	50	0.08	$95.8 \pm 3.5\%$	x	25/ This work
InGaP	PhC (B)	SFWM	2.1×10^5	69	16	$96.6 \pm 4.2\%$	0.17 ± 0.02 (20)	This work

The Q-factor is the loaded one. The internal generation rate is given at 1 mW pump power. For the PhC, B stands for Bichromatic and N for Nanobeam. $g_h^{(2)}(0)$ is given at the corresponding rate [MHz] in parenthesis. They are extracted or deduced from the references.
PPLN periodically poled lithium niobate.

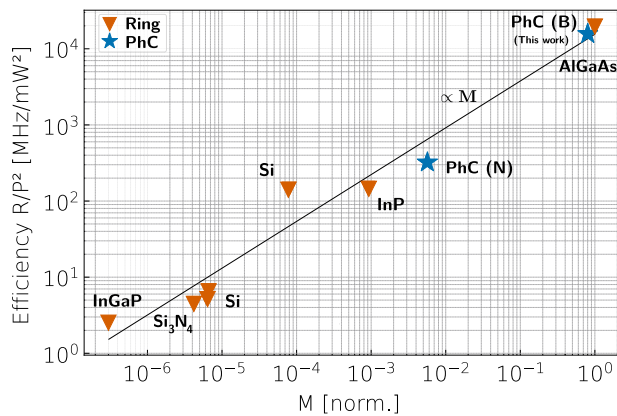


Fig. 5 State-of-the-art of semiconductor photon pair sources based on resonantly enhanced SFWM. Efficiency R/P^2 vs. the normalized figure of merit $M \propto (n_2^2 Q^3)/V^2$ (being 1 for the AlGaAs ring), with Q the Q-factor, V the resonator volume, and n_2 the Kerr nonlinear index. Q and V are deduced from the articles as described in ref. 25. Here, we use $n_2 = 0.6 \times 10^{-17} \text{ m}^2/\text{W}$ for InGaP/Si, $2.7 \times 10^{-17} \text{ m}^2/\text{W}$ for InP, $0.025 \times 10^{-17} \text{ m}^2/\text{W}$ for Si₃N₄⁵¹ and $4 \times 10^{-17} \text{ m}^2/\text{W}$ for AlGaAs. For PhC cavities, N refers to Nanobeam and B to a bichromatic cavity.

power limit, it is necessary to have samples with a minimal mismatch; otherwise the minimum pump power will be set by the amount of dissipation required to compensate for it.

Besides resonant SFWM, we also consider spontaneous parametric down-conversion (SPDC) in Table 2. Relevant figures are the visibility of the Franson fringes and the heralded second-order correlation function at $\tau = 0 : g_h^{(2)}(0)$. Since it is based on second-order nonlinearity, the SPDC process is intrinsically much stronger than SFWM, which is based on a higher-order process. Related to that is also the fact that the scaling with the pump power is different; therefore, a comparison is possible only when fixing either the pump power or the pair generation rate. Here we have chosen the former, consistent with the literature.

First, the data in Table 2 reveal that SFWM sources are almost on par with SPDC. This is essentially due to the fact that the former have lower volumes and higher Q-factors. Yet, exceptionally large SPDC efficiency has been reported in InGaP (the same material as here) rings⁴⁰. This leaves an open question, namely whether the superior intrinsic efficiency of SPDC offsets

the additional complexity: phase matching over one octave, handling very different wavelengths and the tensor nature of second-order processes.

Let us now consider entanglement. From a more practical standpoint, reduced insertion losses and the use of superconducting detectors compared to previous settings²⁵ have considerably improved the detected rate of coincidences (up to 70 kHz), which allows to measure a large amount of entangled photon pairs with integration time as low as 1 s or below. The table reports the net visibility, which does not depend on the interferometer used for the experiment, therefore providing a rather fair comparison of the sources. We report visibility up to 96.6%, which is close to the value measured with the AlGaAs ring²³, yet smaller than in refs. 41,42, where efficiency is much lower.

As for the purity of the heralded photon state, we note that the measurement of the second-order correlation reveals that $g_h^{(2)}(0)$ is not very small. The main reason was that the source was operated at maximal efficiency in order to keep the integration time below three hours. It is well known that single-pair purity decreases when the generation rate increases³⁹ and this is why better results reported elsewhere have been obtained at a much lower generation rate.

Overall, both the visibility of Franson fringes and the purity of the heralded single-photon state are limited by the cavity-detectors losses and unequal Q-factors for the signal and idler modes, which eventually leads to a different count rate on each detector, increasing the background. Substantial improvement is possible by reducing these insertion losses, which are essentially related to the signal and idler separation, and pump suppression. This can be achieved by integrating on-chip these passive linear functions. Another obvious improvement relies on the choice of similar escape rates (loaded Q-factors) for the idler and signal cavity modes. Integration in a complete quantum circuit, as currently pursued with the AlGaAs platform⁴³, is also our perspective; therefore, this engineering work will squarely be addressed in future work.

On a more fundamental standpoint, the demonstration that a PhC resonant parametric source allows entanglement and heralding unlocks the possibility of using photonic bandgap engineering to suppress unwanted photons to a degree which is not accessible to other kind of resonators. In fact, we have shown that it is very easy to operate a PhC resonator such that only the required modes are able to interact through FWM. All the other interactions are strongly suppressed as they correspond to a very low density of

optical states. This has many benefits, for instance, more efficient power conversion in OPOs³⁶, which is more difficult to achieve in ring resonators and requires nontrivial engineering^{44–46}. The suppression of unwanted interactions is also critical for the generation of squeezed light⁴⁷. All these issues are solved using PhC resonators. As a final note, PhC cavities have the lowest footprint (Table 2), which is a direct consequence of the strong confinement. This is an important asset for scalability and the integration of multiple sources on a single chip for photonic computing tasks.

In conclusion, we demonstrated the very efficient generation of time-energy entangled photon pairs using an InGaP photonic crystal cavity. Large efficiency is achieved by operating at low power and scales well compared to most semiconductor-based ring resonators due to a smaller volume. This work proves that PhC cavities are an adequate, different, and competitive candidate for the generation of quantum states of light and can play an important role in integrated quantum optics.

Methods

Sample design, fabrication, and characterization. The samples have been fabricated in the Centre de Nanosciences et de Nanotechnologies (C2N). They consist of an array of 2×11 PhC cavities, fabricated by patterning a suspended membrane of $\text{In}_{0.5}\text{Ga}_{0.5}\text{P}$ lattice-matched to GaAs following the same process as in previous studies²⁹. The layout is transferred using e-beam lithography and then inductively coupled plasma etching (ICP), while wet etching is used to remove the material underlying the membrane.

The cavity, depicted in Fig. 1c, consists of a 2D array of holes with constant period a , except for two lines with a slightly reduced period a' where the cavity is located. A missing line of holes constitutes a waveguide where photons can propagate and are evanescently coupled to the cavity. A mode adapter is placed on the edge of the waveguide to realize an adiabatic transition from the mode of the waveguide to that of the lensed fiber. A reflector is constructed on the other side by shifting inwards two lines of holes.

High-resolution (20 MHz) linear optical spectra are measured using optical coherent tomography (OCT), as detailed in ref. ²⁹. Based on the linear characterization, among the different devices with the proper spectral alignment usable for SFWM, the one with the best trade-off between Q-factors, efficiencies, and spectral misalignment has been selected for nonlinear and quantum measurements.

Experimental setups. The experimental setup for the state generation is depicted in Fig. 6a. A fiber-coupled tunable laser source (Santec TSL-710) is used to pump the process. The sample is stabilized in temperature and accessed through a fiber optical circulator. A lensed fiber is used to couple light in and out of the resonator and the emitted photons, as well as the reflected pump, are collected via the circulator reflection channel. The input polarization is optimized with a polarization controller monitoring the reflected power. When measuring double coincidences to retrieve the internal generation rate, the experimental setup used is in Fig. 6b. The emitted photons are spectrally filtered to attenuate the pump field. The filtering stage consists of a telecom dense wavelength division multiplexing with 3.6 dB of insertion losses and a rejection of 85 dB, and then a tunable bandpass filter per channel, with 3.4 and 4.2 dB of insertion losses, respectively. To measure time correlations, the collected photons are directed into two superconducting nanowire single-photon detectors with a quantum efficiency greater than 85% and a 37 ps time jitter. Details of all the encountered losses by the photons are given in Table 3.

When measuring time-energy entanglement (Fig. 6c), the photons encounter a Franson interferometer. It is a single, fibered, heavily unbalanced Mach-Zehnder interferometer, in which the difference in length between the two arms is $L = 2$ m. The unbalance has to be larger than the coherence length of each of the photons of the emitted pairs $L_{\text{single}}^{\text{coh}}$ (on the order of 10 cm for this device), to wash out classical first-order interference; but simultaneously shorter than the coherence length of the pair, that, in this experiment, is given by the coherence length of the continuous-wave pump laser $L_{\text{pair}}^{\text{coh}}$ (~ 1 km).

The phase is actively stabilized on an ultra-stable laser (Orbits Lightwave Ethereal) with a feedback correction signal sent to a fiber phase shifter. Changing the offset voltage of the phase shifter allows to change the relative phase of the two arms within an estimated error of less than 10° . After leaving the interferometer, the photons encounter the same filtering stage as before. Figure 6d shows the Hanbury Brown-Twiss setup for heralding single photons measurement.

Coincidence peak fitting. We illustrate the heuristic model we adopted to fit the asymmetric coincidence histogram measured in the experimental configurations depicted in Fig. 6b, c. We assume that the emission time of each photon pair is a Poisson point process, but with an average time constant τ_i that is different for the

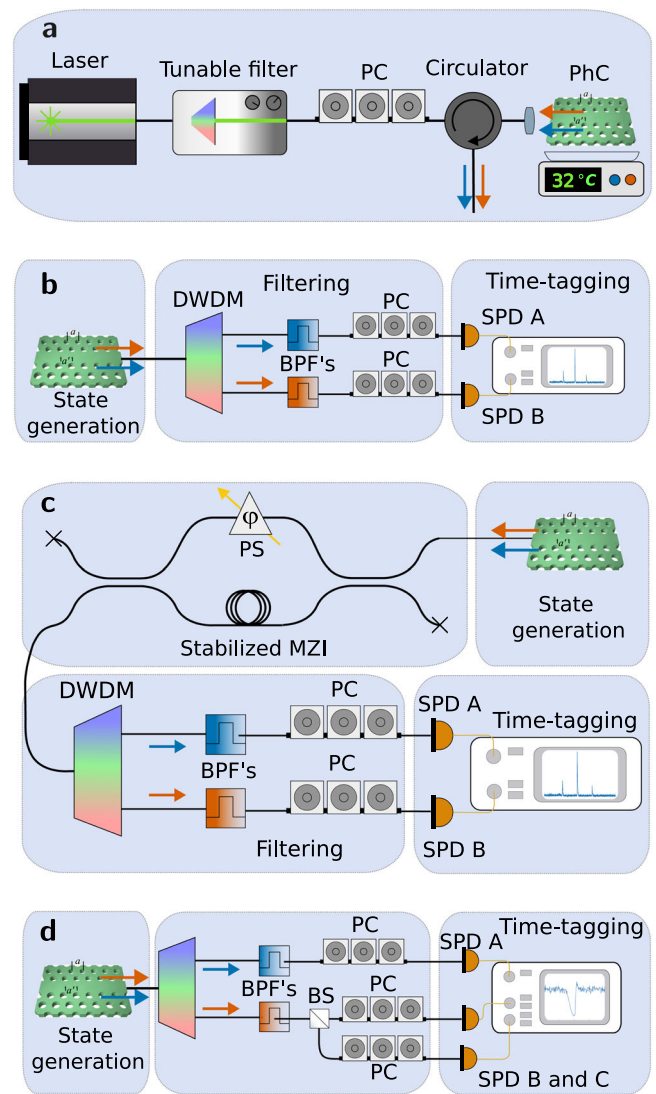


Fig. 6 Experimental setups. **a** Experimental setup for the generation of the photon pairs in the PhC cavity. PC stands for polarization controller. The blue and red arrows denote signal and idler photons. **b** Time-correlation measurement setup. DWDM stands for dense wavelength division multiplexing, BPF for bandpass filter, and SPD for single-photon detector. **c** Time-energy entanglement measurement setup. PS stands for phase shifter, MZI for Mach-Zehnder interferometer. **d** Heralding single-photon emission measurement setup. BS stands for beam-splitter, here with a ratio of 50:50.

signal and idler channel, respectively

$$p_i(t) = \frac{1}{\tau_i} \exp\left(-\frac{t}{\tau_i}\right) \Theta(t) \quad (3)$$

where $\Theta(t)$ is the Heaviside step function. To take into account the time jitter of the detector, we assume a Gaussian time response $g_{\text{jitter}}(t_0 = 0, \sigma)$ with $\sigma = 37$ ps, as characterized by the manufacturer. The probability $p_i(t)$ of measuring a photon at delay t for the signal or idler channel after measuring no photons in the time interval $[0, t]$ is then proportional to the convolution

$$\gamma_i(t) = (g_{\text{jitter}} * p_i)(t) \quad (4)$$

The probability of a coincidence at zero delay is then proportional to the convolution of the probabilities of the independent signal and idler events

$$\Gamma(t, \tau_s, \tau_i) = (\gamma_s * \gamma_i)(t, \tau_s, \tau_i) \quad (5)$$

that is, the lineshape used to fit the coincidence histogram. In Supplementary Note 3 are shown the values of τ_s and τ_i given by the fitting procedure, that

Table 3 Losses (in dB) on the signal and idler channels.

Component	α_s [dB]	α_i [dB]
Chip	2.34	2.34
Circulator + PC	2	2
DWDM	3.6	3.6
BP filter	3.4	4.2
SNSPD	0.7	0.7
Total	12.04	12.84

DWDM dense wavelength division multiplexing, PC polarization controller, SNSPD superconducting nanowire single-photon detectors.

correspond to the dwelling times retrievable from the linewidth of the resonances measured with spectroscopic techniques.

Bell curve data extraction. Using the experimental setup depicted in Fig. 6c, a number of histograms have been acquired for different values of the phase $\varphi_s + \varphi_i$. The same process detailed in section Coincidence peak fitting is used to extract the number of coincidences in each of the three peaks in a typical histogram (see Fig. 3a). The error on the coincidences is assumed here to be Poissonian. The dependence of the coincidence rate R_{det} with $\varphi_s + \varphi_i$ is fitted using the following sinusoidal function as in ref. 21 :

$$f_{(f_0, A, \varphi_0)}(\varphi) = f_0 + A \cos(\varphi + \varphi_0) \quad (6)$$

with f_0 , A , and φ_0 are fit parameters. As a consequence, if R_c is the number of coincidence rate of the central peak, the raw visibility defined as $V_{\text{raw}} = (R_{c,\text{max}} - R_{c,\text{min}})/(R_{c,\text{max}} + R_{c,\text{min}})$ can be directly extracted from the fit parameters using eq. (6) : $V_{\text{raw}} = A/f_0$. The error on each fit parameter is obtained from the covariance matrix giving the standard deviation on the visibility:

$$\frac{\sigma_{V_{\text{raw}}}}{V_{\text{raw}}} = \sqrt{\left(\frac{\sigma_A}{A}\right)^2 + \left(\frac{\sigma_{f_0}}{f_0}\right)^2} \quad (7)$$

Finally, we can deduce the number of standard deviations from which the Bell inequality is violated, knowing entanglement is proved if $V_{\text{raw}} > 70.71\%$.

Data availability

All essential data were available in the paper. Additional data were given in the supplementary file. Further supporting data can be provided from the corresponding author upon request.

Received: 4 November 2022; Accepted: 28 March 2023;

Published online: 18 April 2023

References

- Wehner, S., Elkouss, D. & Hanson, R. Quantum internet: a vision for the road ahead. *Science* **362**, eam9288 (2018).
- Ekert, A. K. Quantum cryptography based on bell's theorem. *Phys. Rev. Lett.* **67**, 661–663 (1991).
- Madsen, L. S. et al. Quantum computational advantage with a programmable photonic processor. *Nature* **606**, 75–81 (2022).
- Slussarenko, S. & Pryde, G. J. Photonic quantum information processing: a concise review. *Appl. Phys. Rev.* **6**, 041303 (2019).
- Bernien, H. et al. Probing many-body dynamics on a 51-atom quantum simulator. *Nature* **551**, 579–584 (2017).
- Arrazola, J. M. et al. Quantum circuits with many photons on a programmable nanophotonic chip. *Nature* **591**, 54–60 (2021).
- Vigliar, C. et al. Error-protected qubits in a silicon photonic chip. *Nat. Phys.* **17**, 1137–1143 (2021).
- Martínez, J. A. et al. Photonic indistinguishability of the tin-vacancy center in nanostructured diamond. *Phys. Rev. Lett.* **129**, 173603 (2022).
- Siampour, H. et al. Ultrabright single-photon emission from germanium-vacancy zero-phonon lines: deterministic emitter-waveguide interfacing at plasmonic hot spots. *Nanophotonics* **9**, 953–962 (2020).
- Wu, C. et al. Room-temperature on-chip orbital angular momentum single-photon sources. *Sci. Adv.* **8**, eabk3075 (2022).
- Uppu, R. et al. Scalable integrated single-photon source. *Sci. Adv.* **6**, eabc8268 (2020).
- da Silva, S. F. C. Gaas quantum dots grown by droplet etching epitaxy as quantum light sources. *Appl. Phys. Lett.* **119**, 120502 (2021).
- Liu, F. et al. High purcell factor generation of indistinguishable on-chip single photons. *Nat. Nanotechnol.* **13**, 835–840 (2018).
- Borghini, M. et al. Superspontaneous four-wave mixing in an array of silicon microresonators. *Phys. Rev. Appl.* **18**, 034007 (2022).
- Sabattoli, F. A. et al. Suppression of parasitic nonlinear processes in spontaneous four-wave mixing with linearly uncoupled resonators. *Phys. Rev. Lett.* **127**, 033901 (2021).
- Jin, B., Mishra, D. & Argyropoulos, C. Efficient single-photon pair generation by spontaneous parametric down-conversion in nonlinear plasmonic metasurfaces. *Nanoscale* **13**, 19903–19914 (2021).
- Chuprina, I., Perminov, N., Tarankova, D. Y. & Kalachev, A. Generating pure single-photon states via spontaneous four-wave mixing in a system of coupled microresonators. *Laser Phys. Lett.* **15**, 105104 (2018).
- Signorini, S. et al. A silicon source of heralded single photons at 2 μm . *APL Photonics* **6**, 126103 (2021).
- Helt, L. G., Liscidini, M. & Sipe, J. E. How does it scale? Comparing quantum and classical nonlinear optical processes in integrated devices. *JOSA B* **29**, 2199–2212 (2012).
- Azzini, S. et al. Ultra-low power generation of twin photons in a compact silicon ring resonator. *Opt. Express* **20**, 23100–23107 (2012).
- Grassani, D. et al. Micrometer-scale integrated silicon source of time-energy entangled photons. *Optica* **2**, 88–94 (2015).
- Kumar, R. R., Raevskaia, M., Pogoretskii, V., Jiao, Y. & Tsang, H. K. Entangled photon pair generation from an InP membrane micro-ring resonator. *Appl. Phys. Lett.* **114**, 021104 (2019).
- Steiner, T. J. et al. Ultrabright entangled-photon-pair generation from an al ga as-on-insulator microring resonator. *PRX Quantum* **2**, 010337 (2021).
- Foresi, J. Photonic-bandgap microcavities in optical waveguides. *Nature* **390**, 143–145 (1997).
- Chopin, A. et al. Time-correlated photons from an $\text{in}_0.5\text{ga}_{0.5}\text{p}$ photonic crystal cavity on a silicon chip. *Phys. Rev. Res.* **4**, 043132 (2022).
- John, S. Strong localization of photons in certain disordered dielectric superlattices. *Phys. Rev. Lett.* **58**, 2486–2489 (1987).
- Akahane, Y., Asano, T., Song, B.-S. & Noda, S. High-Q photonic nanocavity in a two-dimensional photonic crystal. *Nature* **425**, 944–947 (2003).
- Asano, T., Ochi, Y., Takahashi, Y., Kishimoto, K. & Noda, S. Photonic crystal nanocavity with a Q factor exceeding eleven million. *Opt. Express* **25**, 1769 (2017).
- Combrié, S., Lehoucq, G., Moille, G., Martin, A. & De Rossi, A. Comb of high-Q resonances in a compact photonic cavity. *Laser Photonics Rev.* **11**, 1700099 (2017).
- Azzini, S. et al. Stimulated and spontaneous four-wave mixing in silicon-on-insulator coupled photonic wire nano-cavities. *Appl. Phys. Lett.* **103**, 031117 (2013).
- Lian, J. et al. Dispersion of coupled mode-gap cavities. *Opt. Lett.* **40**, 4488–4491 (2015).
- Popović, M. A., Manolatou, C. & Watts, M. R. Coupling-induced resonance frequency shifts in coupled dielectric multi-cavity filters. *Opt. Express* **14**, 1208–1222 (2006).
- Clementi, M., Barone, A., Fromherz, T., Gerace, D. & Galli, M. Selective tuning of optical modes in a silicon comb-like photonic crystal cavity. *Nanophotonics* **9**, 205–210 (2020).
- Marty, G., Combrié, S., Raineri, F. & De Rossi, A. Photonic crystal optical parametric oscillator. *Nat. Photonics* **15**, 53–58 (2021).
- Alpegiani, F., Andreani, L. C. & Gerace, D. Effective bichromatic potential for ultra-high Q-factor photonic crystal slab cavities. *Appl. Phys. Lett.* **107**, 261110 (2015).
- Chopin, A. et al. Canonical four-wave-mixing in photonic crystal resonators: tuning, tolerances and scaling. *IEEE Journal of Selected Topics in Quantum Electronics*, **29**, 1,1–13 (2022).
- Franson, J. D. Bell inequality for position and time. *Phys. Rev. Lett.* **62**, 2205 (1989).
- Signorini, S. & Pavesi, L. On-chip heralded single photon sources. *AVS Quantum Sci.* **2**, 041701 (2020).
- Ma, Z. Ultrabright quantum photon sources on chip. *Phys. Rev. Lett.* **125**, 263602 (2020).
- Zhao, M. & Fang, K. Ingap quantum nanophotonic integrated circuits with 1.5 nonlinearity-to-loss ratio. *Optica* **9**, 258–263 (2022).
- Ma, C. et al. Silicon photonic entangled photon-pair and heralded single photon generation with $\text{car} > 12,000$ and $g^{(2)}(0) < 0.006$. *Opt. Express* **25**, 32995–33006 (2017).
- Oser, D. et al. High-quality photonic entanglement out of a stand-alone silicon chip. *npj Quantum Inf.* **6**, 31 (2020).
- Castro, J. E. et al. Expanding the quantum photonic toolbox in algaaso. *APL Photonics* **7**, 096103 (2022).
- Stone, J. R., Moille, G., Lu, X. & Srinivasan, K. Conversion efficiency in kerr-microresonator optical parametric oscillators: From three modes to many modes. *Phys. Rev. Appl.* **17**, 024038 (2022).

45. Nigro, D., Clementi, M., Brés, C.-S., Liscidini, M. & Gerace, D. Single-photon nonlinearities and blockade from a strongly driven photonic molecule. *Opt. Lett.* **47**, 5348–5351 (2022).
46. Perez, E.F. et al. High-performance Kerr microresonator optical parametric oscillator on a silicon chip. *Nat. Communications*, **14**, 242 (2023).
47. Zhang, Y. et al. Squeezed light from a nanophotonic molecule. *Nat. Commun.* **12**, 1–6 (2021).
48. Xu, B.-Y. et al. Spectrally multiplexed and bright entangled photon pairs in a lithium niobate microresonator. *Sci. China Phys. Mech. Astron.* **65**, 1–7 (2022).
49. Guo, X. et al. Parametric down-conversion photon-pair source on a nanophotonic chip. *Light. Sci. Appl.* **6**, e16249–e16249 (2017).
50. Ramelow, S. et al. Silicon-nitride platform for narrowband entangled photon generation. Preprint at arXiv:1508.04358 (2015).
51. Moody, G., Chang, L., Steiner, T. J. & Bowers, J. E. Chip-scale nonlinear photonics for quantum light generation. *AVS Quantum Sci.* **2**, 041702 (2020).

Acknowledgements

The authors thank Dario Gerace for enlightening discussions and for having encouraged this collaboration. A.D.R. thanks Mikkel Heuck, K. Bensheick, I. Sagnes, and T. Debuisschert for stimulating discussions. This work was funded by the Agence nationale de la recherche (ANR) under the contract COLOURS (ANR-21-CE24-0024) and by Ministero dell’Istruzione, dell’Università e della Ricerca [MIUR grant Dipartimenti di Eccellenza 2018-2022 (F11I18000680001)]. This work was partly supported by the French Renatech network.

Author contributions

A.C. and A.B. equally contributed to the measurements, analysed the data, and wrote the manuscript with the contributions of all the authors. I.G. contributed to the preliminary linear measurements. S.C. contributed to the fabrication of the sample and developed the optical characterization facilities used in TRT. D.B. helped during the quantum experiments. F.R. fabricated the sample. A.D.R., M.G., and F.R. equally supervised the work.

Competing interests

The authors declare no competing interests.

Additional information

Supplementary information The online version contains supplementary material available at <https://doi.org/10.1038/s42005-023-01189-x>.

Correspondence and requests for materials should be addressed to Alexandre Chopin.

Peer review information *Communications Physics* thanks the anonymous reviewers for their contribution to the peer review of this work. Peer reviewer reports are available.

Reprints and permission information is available at <http://www.nature.com/reprints>

Publisher’s note Springer Nature remains neutral with regard to jurisdictional claims in published maps and institutional affiliations.



Open Access This article is licensed under a Creative Commons Attribution 4.0 International License, which permits use, sharing, adaptation, distribution and reproduction in any medium or format, as long as you give appropriate credit to the original author(s) and the source, provide a link to the Creative Commons license, and indicate if changes were made. The images or other third party material in this article are included in the article’s Creative Commons license, unless indicated otherwise in a credit line to the material. If material is not included in the article’s Creative Commons license and your intended use is not permitted by statutory regulation or exceeds the permitted use, you will need to obtain permission directly from the copyright holder. To view a copy of this license, visit <http://creativecommons.org/licenses/by/4.0/>.

© The Author(s) 2023